

Strains and pseudo-magnetic fields in circular graphene rings

Nima Abedpour,¹ Reza Asgari,^{1,*} and F. Guinea²

¹*School of Physics, Institute for Research in Fundamental Sciences, IPM, Tehran 19395-5531, Iran*

²*Instituto de Ciencia de Materiales de Madrid, CSIC,
Sor Juana Inés de la Cruz 3, E-28049 Madrid, Spain*

We demonstrate that circular graphene ring under a shear stress displays strong pseudo-magnetic fields. We calculate the pseudo-magnetic field both from continuum elasticity theory as well as molecular dynamics simulations. Stable wrinkles are induced by shear deformations and lead to enhancement of the pseudo-magnetic field. The strong pseudo-magnetic field found here can be observed by imaging graphene flake at the atomic level *e.g.* through scanning tunneling microscope.

PACS numbers: 61.48.Gh, 81.40.Jj, 07.55.Db

I. INTRODUCTION

Graphene has recently attracted intensive interest as a promising candidate material for the new generation of electronics and spintronics¹. One of the exciting physics on graphene is strain exerted on graphene samples²⁻⁴. It was proposed that strain can be utilized to generate various basic elements for all-graphene electronics³.

Semiconductor quantum rings have been investigated by a number of groups⁵⁻⁹. In graphene ring, the spectrum reveals signatures of effective time-reversal symmetry breaking, in which the spectra are most naturally interpreted in terms of effective magnetic flux contained in the ring, even when no real flux is present. Quantum rings can be considered as prototypical devices in mesoscopic physics, as they show one of the most basic coherence effects, namely the Aharonov-Bohm effect, oscillations of the transmission as a function of the magnetic flux through the ring. The reason for these oscillations is the phase difference between electrons traveling along the different arms of the ring. Furthermore, Benjamin and Pachos¹⁰ proposed creating a ring of single-layer graphene in which they induce d-wave superconductivity via the proximity effect or directly make graphene superconducting by doping. The quantum qubits would be built around the π -junction that naturally occurs in graphene and would not require bilayer structures. The Aharonov Bohm oscillations, on the other hand, has been observed⁹ in a graphene ring, consisting of a planar honeycomb lattice of carbon atoms in a ring shape, by changing the voltage applied to the side gate or the back gate.

When the graphene sheet is under tension, the side contacts induce a long-range elastic deformation which acts as a pseudo-magnetic field for its massless charge carriers^{11,12}. This is because strain changes the bonds length between atoms and affects the way electrons move among them. The pseudo-magnetic field would reveal itself through its effects on electron orbits. The tension can be generated either by the electrostatic force of the underlying gate¹³ by interaction of graphene with the side walls¹⁴, as a result of thermal expansion¹⁵ or by quench height fluctuations¹⁶. A particular strain geometry in graphene could lead to a uniform pseudo-magnetic field and might open up interesting applications in graphene nano-electronics with real magnetic fields¹⁷. Mechanical strains can introduce new environments in studying novel physics of graphene.

It is commonly believed that strains have important influence on the electronic structure of graphene¹⁸. A graphene ring is a particularly convenient geometry. Strains can possibly be manipulated efficiently in samples with good adhesion to the substrate, such as graphene layers grown epitaxially on SiC. Recently, the physical properties of graphene when its hexagonal lattice is stretched out of equilibrium have been investigated by many groups^{19,20}. Scanning tunneling microscopy studies on graphene surface have indeed revealed a correlation between local strain and tunneling conductance²⁰. Motivated by experiments pointing to a remarkable stability of graphene with large strains, we have carried out theoretical analysis and the molecular dynamics simulation to explore the pseudo-magnetic field in strained graphene ring.

In this papers we focus on a particular aspect of the physics of graphene ring namely the appearance of gauge fields and its corresponding pseudo-magnetic fields which arise in the circular graphene ring when a shear force is applied to its boundary. The common belief is that the morphologies of graphene surface under strain are negligible. The aim of this paper is to show that, contrary to these expectations, the structure of a deformed surface can lead to a strong pseudo-magnetic field.

The paper is organized as follows. In Sec. II we introduce our model and formalism. In Sec. III, our numerical results for the strain and the pseudo-magnetic field for deformed graphene ring are presented. Finally, we conclude in Sec. IV with a brief summary.

II. MODEL AND THEORY

We analyze both analytically and numerically the strains and pseudo-magnetic fields in circular graphene ring under a shear stress. A shear force is applied to the boundary, inducing shear deformations inside graphene ring.

The properties of graphene presented lie on the special character of its low energy excitations obeying a two dimensional massless Dirac equation. The graphene ring with valley degree of freedom, $\tau = \pm 1$ for the inequivalent K and K' valleys, is modelled by the massless Dirac Hamiltonian in the continuum model^{21,22}

$$\mathcal{H}_0 = \hbar v_F \tau (\sigma_1 k_1 + \sigma_2 k_2)$$

where k_i is an envelope function momentum operator, $v_F \simeq 10^6 m/s$ is the Fermi velocity, and $\sigma_i = x, y, z$ are the Pauli matrices that act on the sublattice pseudospin degree of freedom. Hence it is important to establish the robustness of the low energy description under small lattice deformations. The concepts of gauge fields and covariant derivatives can be translated into the language of differential geometry, based on differential forms. When ideal graphene is distorted, the effective Hamiltonian will be changed into

$$H = v_F (\mathbf{p} - \mathbf{e} \mathbf{A}) \cdot \boldsymbol{\sigma} \quad (1)$$

where the induced vector potential field is defined through the deformations of sample and \mathbf{p} is the momentum in the polar coordinate. The induced gauge fields can be calculated through the following expressions¹¹

$$\begin{aligned} v_F e A_x &= \hbar g_2 (u_{xx} - u_{yy}) \\ v_F e A_y &= -2\hbar g_2 u_{xy} \end{aligned} \quad (2)$$

with

$$\begin{aligned} g_2 &= \frac{3\kappa\beta}{4} t \\ \kappa &= \frac{\sqrt{2}\mu}{2B} \end{aligned} \quad (3)$$

where $t \approx 2.7$ eV is the nearest-neighbor hopping parameter and $\beta = \partial \ln(t)/\partial \ln(a) \simeq 2$ is the electron Grüneisen parameter. For the shear μ and bulk moduli, B we have used²³ the values $\mu = 9.95$ eV \AA^{-2} and $B = 12.52$ eV \AA^{-2} . We thus find that $\kappa \approx 0.56$. Once the induced gauge field is obtained, the pseudo-magnetic field can be calculated by $\mathbf{B} = \nabla \times \mathbf{A}$.

When the graphene is deformed due to the force exerts on the boundaries, the strain tensor can be calculated from

$$u_{\alpha\beta} = \frac{\partial_\alpha u_\beta + \partial_\beta u_\alpha}{2} + \frac{\partial_\alpha h \partial_\beta h}{2} \quad (4)$$

where \mathbf{u} is the atomic displacement field and h is the out of plane displacement. The contribution of the out-of-plane atomic displacements are noticeable in our numerical calculations.

A. Analytical expression for pseudo-magnetic field

We consider the case of a graphene ring of radius R and width $W = R - R_1$ where the clamped outer and inner boundaries are circles of radius R and R_1 , respectively. Additionally, we assume that the out-of-plane atomic displacements being zero, $h = 0$. The displacement at the outer boundary is $u_\theta(R, \theta) = U_\theta$, $u_r(R, \theta) = 0$, which the shear deformation at the boundary is defined by U_θ , and at the inner boundary we have $u_\theta(R_1, \theta) = u_r(R_1, \theta) = 0$. The displacements in the graphene ring are

$$\begin{aligned} u_r(r, \theta) &= 0 \\ u_\theta(r, \theta) &= U_\theta \left[-\frac{R_1^2 R}{r(R^2 - R_1^2)} + \frac{Rr}{R^2 - R_1^2} \right]. \end{aligned} \quad (5)$$

The second term in the expression for $u_\theta(r, \theta)$ is a pure rotation, required to satisfy the boundary conditions. The only non-zero component of the strain tensor is $u_{r\theta}$. The strain at radius r is

$$u_{r\theta}(r, \theta) = \frac{1}{2} \left(\frac{\partial u_\theta}{\partial r} + \frac{1}{r} \frac{\partial u_r}{\partial \theta} - \frac{u_\theta}{r} \right) = \frac{U_\theta R_1^2 R}{r^2 (R^2 - R_1^2)} \quad (6)$$

The maximum strain at the boundary is actually given by $\bar{u} = U_\theta R / (R^2 - R_1^2)$. Using polar coordinates (r, θ) , Eq. (2) can be rewritten as

$$\begin{aligned} A_r &= \Phi_0 \frac{c\beta}{a} \left[\left(\frac{\partial u_r}{\partial r} - \frac{u_r}{r} - \frac{1}{r} \frac{\partial u_\theta}{\partial \theta} \right) \cos(3\theta) \right. \\ &\quad \left. + \left(-\frac{\partial u_\theta}{\partial r} + \frac{u_\theta}{r} - \frac{1}{r} \frac{\partial u_r}{\partial \theta} \right) \sin(3\theta) \right], \\ A_\theta &= \Phi_0 \frac{c\beta}{a} \left[\left(-\frac{\partial u_\theta}{\partial r} + \frac{u_\theta}{r} - \frac{1}{r} \frac{\partial u_r}{\partial \theta} \right) \cos(3\theta) \right. \\ &\quad \left. + \left(-\frac{\partial u_r}{\partial r} + \frac{u_r}{r} + \frac{1}{r} \frac{\partial u_\theta}{\partial \theta} \right) \sin(3\theta) \right], \end{aligned} \quad (7)$$

where $\Phi_0 = h/2e$ is the quantum unit of magnetic flux and $c = \sqrt{3}\kappa/(2\pi)$ is a constant. Furthermore, the induced gauge field in the polar coordinate is given by

$$\begin{aligned} A_r &= \Phi_0 \frac{c\beta U_\theta}{a} \frac{2R_1^2 R}{r^2(R^2 - R_1^2)} \sin(3\theta) \\ A_\theta &= \Phi_0 \frac{c\beta U_\theta}{a} \frac{2R_1^2 R}{r^2(R^2 - R_1^2)} \cos(3\theta) \end{aligned} \quad (8)$$

Eventually, the pseudo-magnetic field acting on the electrons is simply given by

$$B(r, \theta) = \Phi_0 \frac{c\beta}{a} \frac{8U_\theta R_1^2 R}{r^3(R^2 - R_1^2)} \cos(3\theta) \quad (9)$$

It would be worthwhile mentioning that the pseudo-magnetic field diverges near the clamped sites as $B(r) \approx 8c\Phi_0\beta\bar{u}R_1^2/(ar^3)$.

B. Molecular dynamics simulation

We used Molecular Dynamics simulation (MD) to simulate a suspended circular graphene ring, consists of a planar honeycomb lattice of carbon atoms in a ring shape. Rigidly clamped boundary conditions were employed. We simulated the system at different temperatures by employing Nosè-Hoover thermostat to help the system reach equilibrium at a given temperature. Our present results are limited to $T = 50K$. In this work, we used both the Brenner's bond-order potential^{24,26} incorporating the second nearest neighbors interactions through their dependence on the bond angles and the second-generation reactive empirical bond-order (REBO) potential²⁵ for the carbon-carbon interactions (for more details see Appendix A). It is well established that MD simulations predict the correct mechanical properties and the form of the structures with carbon atoms by using the Brenner potential.

The number of carbon atoms in our simulations is 5125 corresponding to graphene ring of radius $R = 7$ nm and width $W = 4$ nm. At the beginning of calculations, we simulate the circular graphene ring at a given temperature with circular clamped boundary conditions. After reaching a stable configuration, we rotate the outer boundary of graphene ring about $\theta_0 = 12^\circ$ as the system shown in Fig. 1(left panel). For later purposes, we name the system as case one. In this case, the displacement of the boundary atoms is about $U_\theta = R\pi\theta_0/180$. For the sake of comparison, we would like to consider another system in which the inner boundary is pulled down. In the later case, in order to avoid from strong wrinkles, we reduce the rotation of the outer boundary about 6° and then pull slowly down the central part of graphene sheet about $z = -1.7$ nm as shown in Fig. 1(right panel). Again, the latter system is labeled as case two.

III. NUMERICAL RESULTS

From the analytical calculations, the pseudo-magnetic field obtained in the graphene ring geometry where $h = 0$ is shown in Fig. 2. For given the circular radius, $B = 7.89 \times 10^7 \cos(3\theta)/r_0^3$ in units of tesla where r_0 scaled in units of Angstrom. The maximum field occurs in the vicinity of the inner boundary and it decreases like $1/r^3$. Although the analytical model described above can explain the behavior of the strains and magnetic field, we point out that the wrinkle structures represent an important feature of the results.

We use two different systems in the numerical simulations. We first study a graphene ring which is placed in the $x - y$ plane and set at a given temperature by allowing the surface fluctuations in the third dimension, and then the outer boundary of graphene ring is rotated while the inner boundary is clamped as is shown in Fig. 1 (left panel). In case one, we have seen noticeable wrinkle structures around the inner boundary along the perpendicular direction (z -axis). In case two, on the other hand, the graphene ring surface is smoother, but the average carbon-carbon distance is longer than the one obtained in case one. In the following, we will describe two cases and find the pseudo-magnetic fields emerge due to the strains. In our MD simulations, the equations of motion are integrated by the Verlet algorithm with a time step of 0.5 fs. Our numerical results show that the formation of the wrinkles are quantitatively sensitive to the details of the potential. We simulate a system with two mentioned potentials and find that the order of the pseudo-magnetic fields are the same (for more details, see Appendix A). Therefore, we mainly use the Brenner potential²⁴ to calculate the pseudo-magnetic field.

A. Deformed structure

As it can be seen from the left panel of Fig 1, the main part of the deformation occurs in the area near the inner boundary and makes noticeable fluctuations along the z -direction. Due to the appearance of wrinkles in the system, the strain increases near the inner boundary and reduces in the far regions. In contrast to the analytical calculations, the strain does not behave as r^{-2} . The analytical model does not describe well a system with out of plane wrinkles.

In the right panel of Fig 1, we show case two, where the static wrinkles are approximately washed out and seemingly the surface of graphene ring is much smoother than case one. The structure of surface displacements can also be seen in Fig 3. This figure clearly shows that the morphology of the surfaces are enormously different and we expect to have a stronger pseudo-magnetic fields for case one with respect to case two.

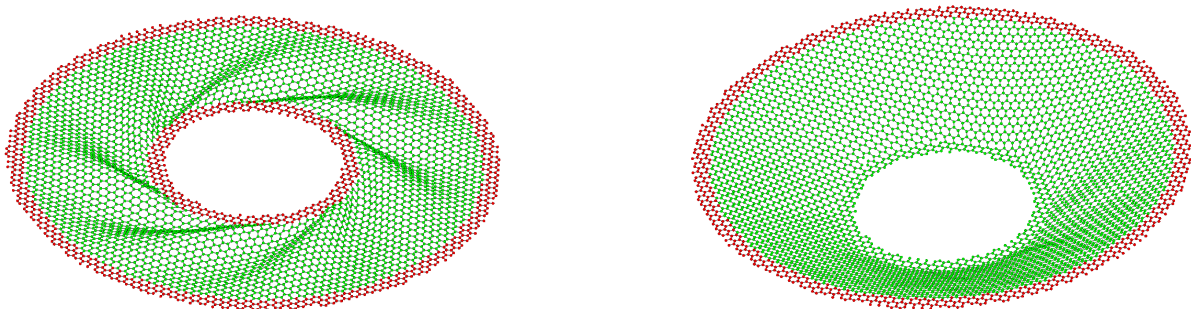


FIG. 1: (Color online) A representative atomic configuration in MD simulations for circular graphene ring at $T = 50$ K. Left panel: case one in which the rotation of the inner boundary is 12° in $x - y$ plane. Right panel, case two in which the inner boundary has been rotated about 6° and afterwards the central part has been pulled down about $z = -1.7$ nm .

It should be noticed that the structure of the simulated samples weakly depend on temperature up to $T = 300$ K.

B. Pseudo-magnetic field

Since the structure of wrinkles, after the relaxation of graphene's shape, is static, we can calculate the gauge fields and also the pseudo-magnetic fields from Eq. (2).

Our numerical results for the induced gauge field calculated from the strains are illustrated in Fig. 4 for two mentioned cases in the $x - y$ plane. We take a time average over the atom positions in order to pass over the thermal fluctuation effects and study only the wrinkling structures. The length value of the vector denotes the absolute value of the gauge field. For case one, the induced gauge fields are not uniform in the area which wrinkles appear.

The pseudo-magnetic field can be calculated from the induced gauge field and its distributions are demonstrated in Fig. 5. It is worth mentioning that the non-zero pseudo-magnetic field, B_z almost occurs along the wrinkles, however its value and structure depends on each wrinkle structure. This is due to the fact that the structure of the wrinkles is different along different lattice directions such as armchair and zigzag. The value of the pseudo-magnetic field that increases with increasing curvature of the wrinkles mostly occur around the central part.

The structure of the pseudo-magnetic field along one of wrinkles, which is indicated in the inset figure, is illustrated in Fig 6 (left panel) for case one. Notice that B_z decreases for $x < 0$ along the wrinkle. The curve can be fitted quite

well with the expression $\exp(-\alpha x)$ where $\alpha = 1.2 \pm 0.1$, which displays fast decaying of the pseudo-magnetic field close to the outer boundary. The pseudo-magnetic field behaves randomly for $x > 0$. The latter behavior is due to the fact that the path is no longer along a specific wrinkle. As it can be observed from the results, the pseudo-magnetic field value is immense. Similar massive pseudo-magnetic fields raised by highly strained nanobubbles that form when graphene is grown on a platinum surface have been measured by Levy *et al.*²⁷.

For case two, which wrinkles are disappeared, the symmetry of the graphene is clearly induced in the B_z , (see Fig 5, right panel).

In order to have a better understanding regarding the structure of the pseudo-magnetic fields, we calculate the pseudo-magnetic fields for two cases along the azimuthal angle at given radius, r . Fig. 7, shows the pseudo-magnetic field B_z as a function of θ around a ring for radius $r = 4$ nm in case one (left panel) and moreover the pseudo-magnetic field is shown at $r = 6.5$ nm for case two (right panel). In the latter case, we have seen the behavior most likely as $B_z \propto \cos(3\theta)$. In this figure, we have plotted function, which is proportional to $\cos(3\theta)$ as solid lines. Apparently the result in the left panel refers to case one behaves similarly to case two with respect to the azimuthal variable, however there are detectable fluctuations due to the appearance of the wrinkles.

The analytical expression of the pseudo-magnetic field acting on the electrons is $B(r, \theta) \propto \frac{1}{r^3} \cos(3\theta)$ when atomic out-of-plane displacements are ignored. The expression was obtained for a system that lies in the $x - y$ plane, $h = 0$, where there are no wrinkle structures on the flake. Since case two, which has less wrinkle structures, is somehow similar to the aforementioned system, we have found numerically the $\cos(3\theta)$ dependence for the pseudo-magnetic field. However due to the fact that the inner boundary is pulled down, the pseudo-magnetic field behaviors differently as a function of r .

IV. CONCLUSIONS

In summary, we have investigated the strains and pseudo-magnetic fields in circular graphene ring under a shear stress. We find, from the elastic theory, the induced gauge field as function of the maximum strain at the boundary, \bar{u} . The magnitude of the pseudo-magnetic field near the boundary is $B \approx 4\sqrt{3}\Phi_0\beta\kappa\bar{u}/(\pi aR)$. Moreover, The field diverges near the clamped sites as $B(r) \propto 1/r^3$, where r is the distance to the site while the strains diverge as $1/r^2$. From numerical simulation results, we find wrinkles structures on graphene flakes and the pseudo-magnetic field is the same order of magnitude that obtained by analytical calculations. We also find that the wrinkle structures represent an important feature of the pseudo-magnetic field. In addition, it is also shown that the pseudo-magnetic field behaves like as $\cos(3\theta)$. These results are essential for understanding the electronic properties of graphene ring and its strain engineering for potential applications.

V. ACKNOWLEDGMENTS

We thank A. Fognini and A. Naji for their useful comments. This research was supported in part by the Project of Knowledge Innovation Program (PKIP) of Chinese Academy of Sciences, Grant No. KJCX2.YW.W10. F. G. is supported by by MICINN (Spain), grants FIS2008-00124 and CONSOLIDER CSD2007-00010.

Appendix A: Empirical potentials

We used both the Brenner's bond-order potential²⁴ incorporating the second nearest neighbors interactions through their dependence on the bond angles and the second-generation reactive empirical bond-order (REBO) potential²⁵ for the carbon-carbon interactions. The latter potential is based on the empirical bond-order formalism and allows for covalent bond binding and breaking with associated changes in the atomic hybridization. Consequently, such a classical potential allows to model complex chemistry in large many-atom systems. The Brenner bond-order potential can be written in the following general form for the binding energy,

$$E_b = \sum_i \sum_{j>i} \{V^R(r_{ij}) - b_{ij}V^A(r_{ij})\} \quad (\text{A1})$$

The first term is repulsive, and the second one is attractive. r_{ij} is the distance between pairs of nearest-neighbor atoms i and j . Although this expression is a simple sum over bond energies, it is not a pair potential since the b_{ij} , which is called the bond-order factor, is in essence a many-body factor. The many-body nature of b_{ij} makes the bond energy depend on the local environment of the bond. This feature allows the Brenner potential to predict correct

geometries and energies for many different carbon structures. The empirical bond-order function used here is written as a sum of terms $b_{ij} = [b_{ij}^{\sigma-\pi} + b_{ji}^{\sigma-\pi}]/2 + b_{ij}^{\pi}$, where values for the functions $b_{ij}^{\sigma-\pi}$ and $b_{ji}^{\sigma-\pi}$ depend on the local coordination and bond angles for atoms i and j , respectively. The first term is a function of the bond angles similar to that in the Brenner potential²⁴ while the second term incorporates the third nearest neighbors via a bond-order term associated with the dihedral angles and becomes nonzero upon bending of the graphene sheets. The values for all the parameters used in our calculation for the potentials can be found in Refs. 24,25 and are therefore not listed here.

We used the Brenner potential²⁶ and alternatively the REBO potential by using Large-scale Atomic or Molecular Massively Parallel Simulator package²⁸ (LAMMPS) for carrying out the molecular dynamic simulations in this work. We calculated the pseudo-magnetic fields for the two different potentials along the azimuthal angle at given radius, $r \simeq 40\text{\AA}$. Fig. 8, shows the pseudo-magnetic fields B_z as a function of θ along a circular ring of radius $r = 4\text{ nm}$. Note that the order of the pseudo-magnetic field is the same in both cases and moreover, we see the same envelop behavior at long-wavelength region. However, they exhibit different oscillations modes at short wavelength due to the way in which the bond-order (the dihedral angle) is handled in the REBO potential.

Appendix B: Simulation methods

Computer simulations generates very detailed information at the microscopic level and the conversion of this information into macroscopic level is the province of statistical mechanics. Molecular dynamics, on the other hand, is an important tool to investigate the microscopic behaviors by integrating the motions of particles or particle clusters. In the molecular dynamics, the trajectories of atoms are determined by numerically solving Newton's equations of motion for a many-body interacting systems, where forces between the particles and their potential energy are defined by certain force fields. We used NVT ensemble where the system is isolated from changes in moles (N), volume (V) and temperature (T). In NVT, the energy of endothermic and exothermic processes is exchanged with a thermostat. A variety of thermostat methods is available to add and remove energy from the boundaries of a MD system in a nearly realistic way, approximating the canonical ensemble. On the other hand, a micro-canonical molecular dynamics trajectory may be seen as an exchange of potential and kinetic energy, with total energy being conserved. For every time step, each particle's position and velocity may be integrated with a method such as Verlet. Given the initial positions and velocities, all future positions and velocities can be calculated. If there is a large enough number of atoms, statistical temperature can be estimated from the instantaneous temperature, which is found by equating the kinetic energy of the system to $nk_B T/2$ where n is the number of degrees of freedom of the system.

We simulated the system at nonzero temperatures by employing a Nosé-Hoover thermostat and the time step is taken as 0.5 fs. At the beginning of the simulation, we consider a circular graphene ring incorporating atoms which are located in the $x - y$ plane. The initial structures are firstly optimized giving the carbon-carbon bond length of 1.45 Å and all samples are initially relaxed at a desired temperature for a duration 1.5 ns. In atomic positions at the boundaries, we enforce $z = 0$ to prevent atomic motion along the z direction and furthermore, after some simulation run-times, we set $x = y = \text{const.}$ to clamp atoms.

-
- * Electronic address: asgari@ipm.ir
- ¹ A. K. Geim, K. S. Novoselov, Nature Material **6**, 183 (2007) .
 - ² M. A. H. Vozmediano, M. I. Katsnelson, F. Guinea, Phys. Reports **496**, 109 (2010) .
 - ³ V. M. Pereira, A. H. Castro Neto, Phys. Rev. Lett. **103**, 046801 (2009) .
 - ⁴ F. Guinea, M. I. Katsnelson, A. K. Geim, Nature Physics **6**, 30 (2010) .
 - ⁵ M. Bayer, M. Korkusinski, P. Hawrylak, T. Gutbrod, M. Michel and A. Forchel, Phys. Rev. Lett. **90**, 186801 (2003) .
 - ⁶ E. Ribeiro, A. O. Govorov, W. Carvalho, Jr. and G. Medeiro-Ribeiro, Phys. Rev. Lett. **92**, 126402 (2004) .
 - ⁷ Saverio Russo, Jeroen B. Oostinga, Dominique Wehenkel, Hubert B. Heersche, Samira Shams Sobhani, Lieven M. K. Vandersypen, and Alberto F. Morpurgo, Phys. Rev. B **77**, 085413 (2008) .
 - ⁸ Jai Seung Yoo, Yung Woo Park, Viera Skakalova, and Siegmund Roth, Appl. Phys. Lett. **96**, 143112 (2010) .
 - ⁹ Magdalena Huefner, Françoise Molitor, Arnhild Jacobsen, Alessandro Pioda, Christoph Stampfer, Klaus Ensslin, and Thomas Ihn, New Journ. Phys. **12**, 043054 (2010) .
 - ¹⁰ Colin Benjamin, Jiannis K. Pachos, Phys. Rev. B **79**, 155431 (2009) .
 - ¹¹ H. Suzuura and T. Ando, Phys. Rev. B **65**, 235412 (2002) .
 - ¹² J. L. Maès, Phys. Rev. B **76**, 045430 (2007) .
 - ¹³ M. M. Fogler, F. Guinea, and M. I. Katsnelson, Phys. Rev. Lett. **101**, 226804 (2008) .
 - ¹⁴ J. S. Bunch, S. S. Verbridge, J. S. Alden, A. M. van der Zande, J. M. Parpia, H. G. Craighead, and P. L. McEuen, Nano Lett. **8**, 2458 (2008) .

- ¹⁵ W. Bao, F. Miao, Z. Chen, H. Zhang, W. Jang, C. Dames, and C. N. Lau, *Nat. Nanotechnol.* **4**, 562 (2009) .
- ¹⁶ F. Guinea, Baruch Horovitz, and P. Le Doussal *Phys. Rev. B* **77**, 205421 (2008) .
- ¹⁷ Tony Low, F. Guinea, *Nano Lett.* **10**, 3551 (2010) .
- ¹⁸ A. H. Castro Neto, F. Guinea, N. M. R. Peres, K. S. Novoselov, and A. K. Geim , *Rev. Mod. Phys.* **81**, 109 (2009) .
- ¹⁹ Keun Soo Kim, Yue Zhao, Houk Jang, Sang Yoon Lee, Jong Min Kim, Kwang S. Kim, Jong-Hyun Ahn, Philip Kim, Jae-Young Choi, and Byung Hee Hong, *Nature* **457**, 706 (2009); T. M. G. Mohiuddin, A. Lombardo, R. R. Nair, A. Bonetti, G. Savini, R. Jalil, N. Bonini, D. M. Basko, C. Galiotis, N. Marzari, K. S. Novoselov, A. K. Geim, and A. C. Ferrari, *Phys. Rev. B* **79**, 205433 (2009); Changgu Lee, Xiaoding Wei, Jeffrey W. Kysar, and James Hone, *Science* **321**, 385 (2008); Mingyuan Huang, Hugen Yan, Tony F. Heinz, and James Hone *Nano Lett.* **10**, 4074 (2010) .
- ²⁰ M. L. Teague, A. P. Lai, J. Velasco, C. R. Hughes, A. D. Beyer, M. W. Bockrath, C. N. Lau, N. C. Yeh, *Nano Lett.* **9**, 2542 (2009) .
- ²¹ J. C. Slonczewski and P. R. Weiss, *Phys. Rev.* **109**, 272 (1958) .
- ²² F. D. M. Haldane, *Phys. Rev. Lett.* **61**, 2015 (1988) .
- ²³ K.V. Zakharchenko, M.I. Katsnelson, and A. Fasolino, *Phys. Rev. Lett.* **102**, 046808 (2009) .
- ²⁴ D. W. Brenner, *Phys. Rev. B* **42**, 9458 (1990) .
- ²⁵ D. W. Brenner, O. A. Shenderova, J. A. Harrison, S. J. Stuart, B. Ni, and S. B. Sinnott, *J. Phys.: Condens. Matter* **14**, 783 (2002) .
- ²⁶ N. Abedpour, M. Neek-Amal, R. Asgari, F. Shahbazi, N. Nafari, and M.R. Tabar, *Phys. Rev. B* **76**, 195407 (2007); N. Abedpour, R. Asgari, and M.R. Tabar, *Phys. Rev. Lett.* **104**, 196804 (2010) .
- ²⁷ N. Levy, S. A. Burke, K. L. Meaker, M. Panlasigui, A. Zettl, F. Guinea, A. H. Castro Neto and M. F. Crommie, *Science* **329** , 554 (2010) .
- ²⁸ "LAMMPS Molecular Dynamics Simulator". Sandia National Laboratories.

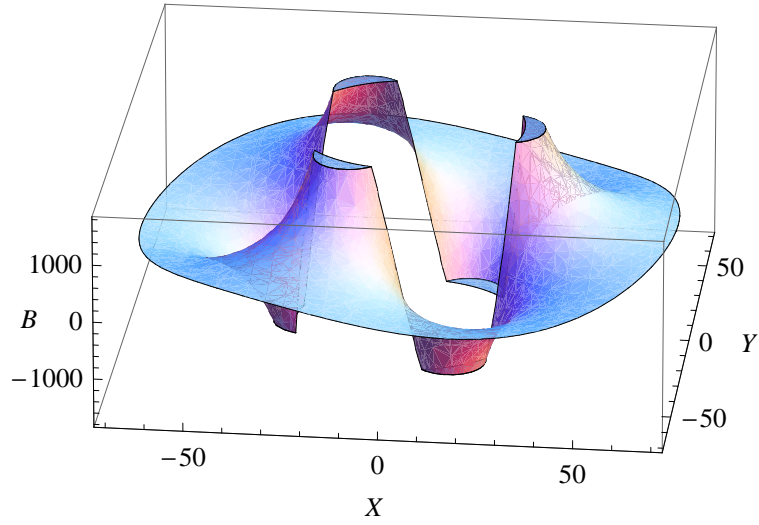


FIG. 2: (Color online) Pseudo-magnetic field, given by Eq. 9 in units of tesla induced by shear strains in a circular graphene ring. Here, $R = 70$, $R_1 = 30\text{\AA}$ and $\theta = 12^\circ$.

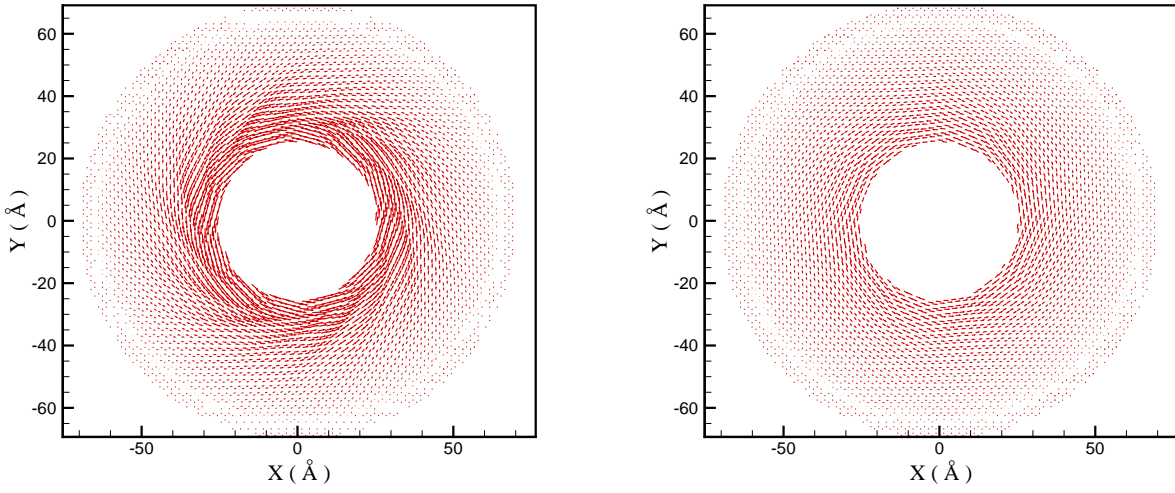


FIG. 3: (Color online) Projected atomic displacements for the case one, left panel and case two, right panel.

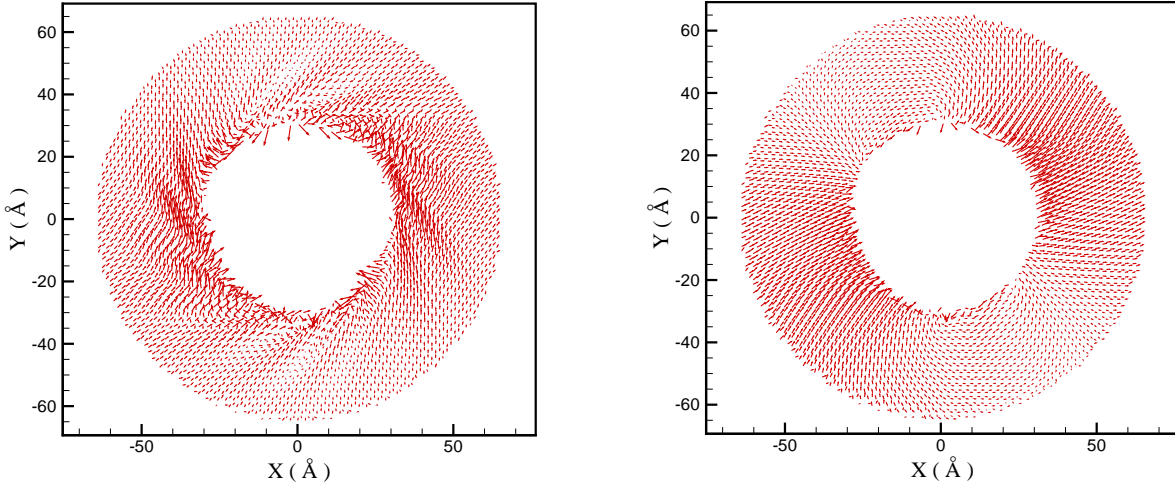


FIG. 4: (Color online) Projected the gauge field, A_μ for two mentioned cases. Notice that the length value of the vector denotes the absolute value of the gauge field.

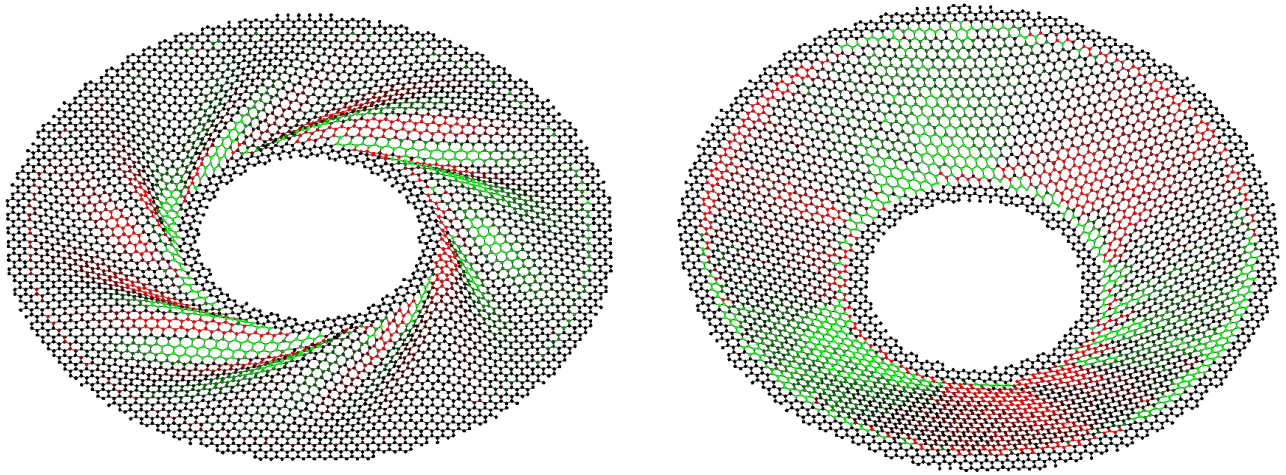


FIG. 5: (Color online) Distribution of the pseudo-magnetic field, B_z on graphene ring for two mentioned cases. Green, red and black colors correspond to positive, negative and zero values of the pseudo-magnetic field, respectively. For the case one, the dark-green(or dark-red) correspond to the strongest pseudo-magnetic field which is about $1000T$ and for the case case two, it is about $200T$

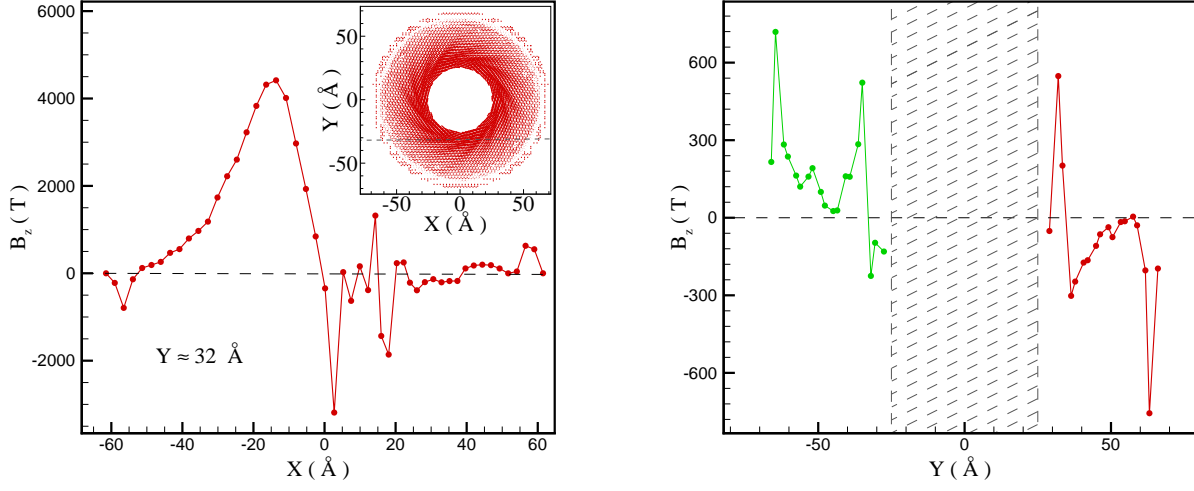


FIG. 6: (Color online) Pseudo-magnetic field, B_z on a specific direction indicates in the inset figure, left panel, and along y -direction passing the origin of the ring, right panel.

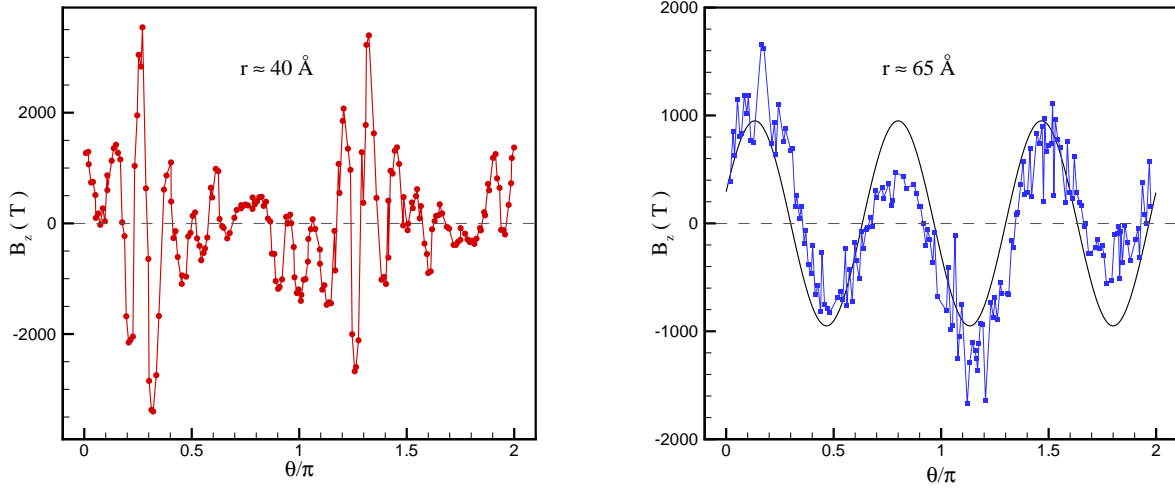


FIG. 7: (Color online) Pseudo-magnetic field, B_z as a function of azimuthal angle for case one at $r = 4 \text{ nm}$, left panel and $r = 6.5 \text{ nm}$ for case two(right panel). Solid line curve denotes a function which is proportional to $\cos(3\theta)$.

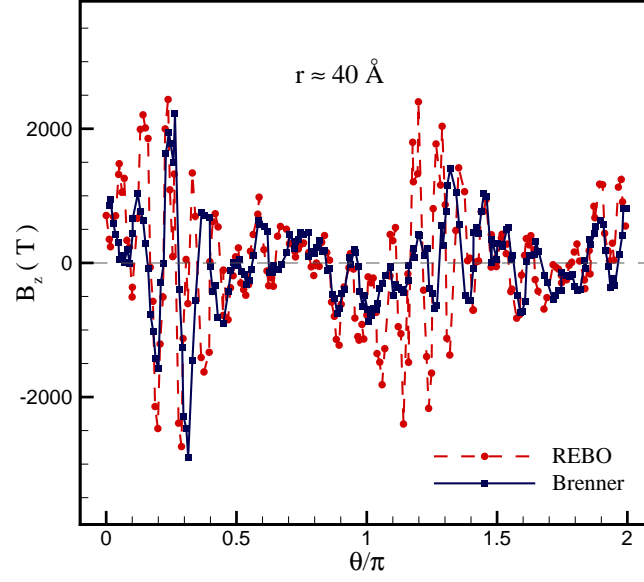


FIG. 8: (Color online) Pseudo-magnetic field, B_z as a function of azimuthal angle at $T = 50K$ along a circular ring of radius 4 nm when the Brenner potential²⁴ and the REBO potential²⁵ are used. Their long-wavelength behavior is very similar to the form $B_z \propto \cos(3\theta)$, however their short wavelength behavior is different due to the way in which the bond-order is handled in the REBO potential. The outer boundary of graphene ring, in both cases, is rotated about $\theta_0 = 8^\circ$.